Ion-ion dynamic structure factor, acoustic modes, and equation of state of two-temperature warm dense aluminum

L. Harbour,[1,*] G. D. Förster,[1] M. W. C. Dharma-wardana,[2,†] and Laurent J. Lewis[1,‡]

[1]*Département de Physique and Regroupement Québécois sur les Matériaux de Pointe, Université de Montréal,*
C.P. 6128, Succursale Centre-Ville, Montréal, Québec, Canada H3C 3J7
[2]*National Research Council of Canada, Ottawa, Ontario, Canada K1A 0R6*

The ion-ion dynamical structure factor and the equation of state of warm dense aluminum in a two-temperature quasiequilibrium state, with the electron temperature higher than the ion temperature, are investigated using molecular-dynamics simulations based on ion-ion pair potentials constructed from a neutral pseudoatom model. Such pair potentials based on density functional theory are parameter-free and depend directly on the electron temperature and indirectly on the ion temperature, enabling efficient computation of two-temperature properties. Comparison with *ab initio* simulations and with other average-atom calculations for equilibrium aluminum shows good agreement, justifying a study of quasiequilibrium situations. Analyzing the van Hove function, we find that ion-ion correlations vanish in a time significantly smaller than the electron-ion relaxation time so that dynamical properties have a physical meaning for the quasiequilibrium state. A significant increase in the speed of sound is predicted from the modification of the dispersion relation of the ion acoustic mode as the electron temperature is increased. The two-temperature equation of state including the free energy, internal energy, and pressure is also presented.

I. INTRODUCTION

The challenge of modeling warm dense matter (WDM)—a system of strongly coupled classical ions and partially degenerate electrons at high temperature and high density—is central to understanding many physical systems such as the interior of giant planets [1], laser machining and ablation [2], and inertial-confinement fusion [3]. In WDM, neither the kinetic energy nor the potential energy can be treated as a perturbation. Hence the usual theoretical techniques of classical plasma physics or solid-state physics become inapplicable. In the laboratory, WDM can be created through the interaction of high-energy short-pulse lasers with simple metals such as aluminum [4,5] and beryllium [6], with densities ρ several times the room density ρ_0 and temperatures of the order of 1 eV. The importance of treating these systems as two-temperature WDM systems rather than equilibrium systems has not always been appreciated in analyzing the experimental results [7,8].

The ion-ion dynamic structure factor (DSF) $S(\mathbf{k},\omega)$ is a key quantity for understanding the WDM regime. For instance, it contains information on the longitudinal waves propagating in the system. The DSF can be measured by neutron scattering and indirectly via x-ray Thomson scattering (XRTS) [9]. The Chihara decomposition [10] has been applied to describe the XRTS signal by partitioning the total electron-electron DSF $S_{ee}(\mathbf{k},\omega)$ in the following form:

$$S_{ee}(\mathbf{k},\omega) = S_{ee}^0(\mathbf{k},\omega) + N(\mathbf{k})S_{ii}(\mathbf{k},\omega) + S_{ee}^{fb}(\mathbf{k},\omega). \quad (1)$$

Here S_{ee}^0 is the free electron-electron DSF, S_{ee}^{fb} is the contribution from transitions between bound and free electrons, $N(\mathbf{k}) = n_b(\mathbf{k}) + n_f(\mathbf{k})$ is the total electron form factor split into a bound part n_b and a free part n_f, and S_{ii} is the ion-ion DSF. Using this decomposition, simulations combining standard density functional theory (DFT) with molecular-dynamics (MD) simulations have been used [4,5,11,12] to extract properties of WDM systems such as the free-electron density per ion n_e (i.e., $\bar{Z}$), the ion density ρ, the electron temperature T_e, and the ion temperature T_i. Since these simulations are computationally expensive, the use of a simpler approach such as the neutral pseudoatom (NPA) model is appropriate. The NPA is well adapted to extract the ion part of the XRTS signals [8] and will be the principal method used in this work, where we show that the NPA also has the needed accuracy. The XRTS spectrum can be computed in the NPA, and also by other means without using the Chihara decomposition [13,14], but its discussion is not needed for this work.

However, the separation between ion acoustic modes $\Delta\omega = 2\hbar\omega_p$, with ω_p the ion-plasma frequency, is of the order of 1 meV, significantly lower than the bandwidth of any x-ray probe laser used experimentally at the moment. Thus, the ion-ion DSF is usually approximated by its static form $S(k,\omega) = S(k)\delta(\omega)$ in describing the XRTS signal. Nevertheless, the ion-ion DSF contains important information about the ion transport properties linked to electron-ion equilibration, the formation of coupled modes, interaction with projectiles, etc., which makes it a key quantity for fully understanding the WDM regime. With x-ray laser sources being improved, the ion-ion DSF should become available from future experiments, motivating its calculation for both equilibrium and quasiequilibrium situations.

*louis.harbour@umontreal.ca
†chandre.dharma-wardana@nrc-cnrc.gc.ca
‡laurent.lewis@umontreal.ca

Furthermore, in the limit of small wave vectors, $k \to 0$, the ion-ion DSF can be described in a hydrodynamic framework [15] (see below), providing important physical quantities such as the adiabatic velocity of sound, the ion acoustic dispersion relation, the thermal diffusivity, and the sound attenuation coefficient. In addition, in the case of simple metals commonly probed in most XRTS experiments, the laser interacts mainly with the free-electron subsystem, creating a nonequilibrium system in which the electron temperature T_e is higher than the initially cold ions at temperature T_i. It has been shown that, when the shock wave resulting from the laser pulse has propagated through the sample and reaches the probing location, the system might still be in a two-temperature ($2T$) state [7,8]. Since the ion-ion interactions in simple metals are related to the screening of the free-electron subsystem, the quasiequilibrium properties of the total system with $T_e \neq T_i$ differ significantly from the equilibrium ones. The hardening of the phonon spectra in ultrafast matter [16–18], where T_e is about 1 eV while T_i remains at room temperature T_r, is an example of how the ion dynamics can be affected drastically in such conditions. Transport properties of Al in the two-temperature regime, such as self-diffusion and shear viscosity, are also significantly modified [19].

The ion-ion DSFs for WDM have been calculated mainly using DFT coupled to classical molecular-dynamics (MD) [11] simulations. Since DSF calculations require a large number of particles and long simulation times, DFT-MD calculations are computationally very intensive. In addition, the finite-T treatment of the electronic subsystem in DFT requires the solution of the Kohn-Sham equations for many electronic bands to take thermal excitations according to the Fermi-Dirac distribution into account. Orbital-free (OF) DFT simulations do not require electronic wave functions, but they do require a Hohenberg-Kohn kinetic-energy functional as well as a finite-T generalization thereof. Such procedures are less accurate than the Kohn-Sham method, but they make the simulations practical [20]. The full DFT-MD simulations when feasible can be used to benchmark simpler methods such as the NPA or OF approaches, which are easily applied over a wider range of temperatures and densities.

In the present work, we compute the ion-ion DSF using classical MD simulations based on pair potentials (PP) constructed from the NPA model, which is fully based on DFT. The NPA approach has already been used to predict the DSF of strongly coupled hydrogen plasmas [21] and provides the sound velocity, the thermal diffusivity, the specific-heat ratio, and the viscosity. The NPA-PPs are free of *ad hoc* parameters and are accurate to within a few meV as established by the prediction of accurate experimental phonon spectra for simple WDM solids [16,17]. The NPA-PP predictions for static structure factors (SSFs) obtained using the modified-hypernetted-chain (MHNC) approximation are in agreement with DFT-MD simulations for WDM systems (typical examples are Be and Al [8]; for a review of the NPA, see Ref. [22]).

Furthermore, in the quasiequilibrium case, i.e., when T_e is different from T_i, the extension of the NPA approach to two-temperature ($2T$) situations has enabled the construction of $2T$-PPs, which reproduce *ab initio* calculations of quasiequilibrium phonon spectra [17], quasiequilibrium XRTS signals [8], and frequency-dependent $2T$ plasmon profiles [7]

and conductivities of ultrafast matter [23]. The objective of the present study is to determine the DSF $S(k,\omega,T_e,T_i)$ in the $2T$ regime. In addition, we evaluate the $2T$ equation of state (EOS). All calculations are carried out for aluminum at the "room-temperature" density of $\rho_0 = 2.7$ g/cm^3 with the ion temperature fixed at $T_i = 1$ eV while the electron temperature T_e is varied between 1 and 10 eV.

II. METHODS

A. Neutral-pseudoatom model

The NPA model [24–26] is a rigorous all-electron DFT average-atom approach in which the ion distribution is also treated in DFT [27]. Given the mean free-electron density n and electron temperature T_e, it determines the total electron density around a *single Kohn-Sham ion* constructed from a nucleus of charge Z_n embedded in the plasma environment of mean density ρ. A classical Kohn-Sham equation for the ions determines the one-body ion distribution $\rho(r) = \rho g_{ii}(r)$, where $g_{ii}(r)$ is the ion pair distribution function (PDF), abbreviated to $g(r)$. The classical Kohn-Sham equation for the ions is identified as a type of hypernetted chain (HNC) integral equation bringing in ion-ion correlations beyond the mean-field approximation. The Kohn-Sham-Mermin solutions are obtained in the local-density approximation using a finite-T_e free-energy exchange-correlation (XC) functional $F_{xc}[n,T_e]$ [28]. The available finite-T XC functionals, fitted to quantum Monte Carlo results or to the classical-map HNC results (used here), yield numerically equivalent results in WDM applications [29].

To simulate the effect of the ion-density $\rho(r)$ on the electronic states, a uniform positive neutralizing background with a spherical cavity of radius r_{ws}, with the nucleus at the origin, is used. Here, $r_{ws} = [3/(4\pi\rho)]^{1/3}$ is the Wigner-Seitz radius of the ion. This lowest-order model for $\rho(r) = \rho g(r)$ is sufficient for calculating the Kohn-Sham energy levels of "simple metal" ions immersed in a warm dense electron fluid, as has been discussed in a recent review [22]. The adjustment of the ion distribution to the electron distribution is accomplished by the optimization of a single parameter, viz. r_{ws}, subject to the finite-T Friedel sum rule [27]. Although, strictly speaking, an electron-ion exchange-correlation functional is also needed [30], it is neglected here.

An advantage of the NPA model is that it directly provides single-ion properties such as the mean ionization $\bar{Z}$ and the electron density around the nucleus $n(r) = n_b(r) + n_f(r)$, with n_b and n_f the bound- and free-electron densities, respectively. In simple metals, n_b is found to be localized within a radius much smaller than r_{ws}, such that $n_b(r \to r_{ws}) = 0$, which enables a clear definition of the mean ionization $\bar{Z} = n - n_b$. Note, however, that the free-electron distribution is *not* restricted to the WS sphere, as is done in many average-atom (AA) models, as reviewed by, e.g., Murillo *et al.* [31].

The free electrons occupy the whole space, modeled by a large correlation sphere of radius R_c of about 10 WS radii, usually sufficient to include all particle correlations associated with the central nucleus. Unlike in AA models, the mean number of free electrons per ion, viz. $\bar{Z}$, is an unambiguously defined quantity subject to the Friedel sum rule, and

experimentally measurable using XRTS [9], static conductivities, Langmuir probes, etc. The interaction among ions of charge $\bar{Z}$ is screened by the free-electron subsystem, which is assumed to respond linearly to the electron-ion pseudopotential

$$U_{ei}(k,T_e) = n_f(k)/\chi(k,T_e). \tag{2}$$

Since $n_f(k)$ is determined by the Kohn-Sham calculation, which goes beyond the linear response to $\bar{Z}/r$, the above pseudopotential actually includes all the nonlinear DFT effects within a linearized setting. The limits of validity of this procedure are discussed in Ref. [32].

With $n_f(k)$ at hand, U_{ei} is constructed using the finite-T interacting electron response function

$$\chi(k,T_e) = \frac{\chi_0(k,T_e)}{1 - V(k)[1 - G(k,T_e)]\chi_0(k,T_e)} \tag{3}$$

with χ_0 the finite-T noninteracting Lindhard function, $V(k) = 4\pi/k^2$ the bare Coulomb interaction, and G a finite-T local-field correction [16], which depends directly on F_{xc}. Finally, the screened ion-ion pair interaction is given by

$$V_{ii}(k,T_e) = \bar{Z}^2 V(k) + |U_{ei}(k,T_e)|^2 \chi(k,T_e). \tag{4}$$

This pair potential is the NPA input to the classical MD calculations.

It should be noted that the NPA uses a pair potential for the ions and does not attempt to include multi-ion potentials, as is customary in effective-medium (EM) approaches that have been successfully used for metals and semiconductors, especially at ambient temperature and compression. The EM method is at best a non-self-consistent DFT approach [33] that includes two-body, three-body, and other multi-ion effects. It is often further extended by fitting to empirical and calculational databases. However, recent attempts to use such models for, e.g., WDM carbon, have not been very successful [34]. The NPA approach exploits the fact that the grand potential $\Omega[n,\rho]$ is a functional of *both* the one-electron distribution $n(r)$ and the one-ion distribution $\rho(r)$. Hence a single-ion description (which allows a pair potential) is the only rigorously necessary information for a full DFT description of the system. In practice, pair potentials are sufficient if linear-response pseudopotentials could be constructed, as in Eq. (2). However, this approach now needs not only an XC functional for the electrons but also a correlation functional for the classical ions. These are constructed via classical integral equations, or automatically via MD simulations. Detailed discussions of these issues and the NPA method may be found in Refs. [22,35]. In this context, we remark that standard implementations of DFT-MD in codes like ABINIT and VASP [36,37] use only the one-electron density-functional property, and *not* the one-ion density functional, as it chooses to implement a full N-ion Kohn-Sham simulation with N typically of the order of 100 or more.

Furthermore, the multicenter nature of the simulations implies a highly nonuniform electron density requiring sophisticated gradient-corrected XC functionals. In contrast, the NPA uses a relatively smooth single-center electron distribution for which the local-density approximation (LDA) is found to work very well, even for sensitive properties such as the electrical conductivity [23] and plasmon spectral line shapes

[7]. The LDA form of the finite-T XC functional of Perrot and Dharma-wardana [28] is used in this study.

B. Dynamic structure factor

The ion-ion spatial and temporal correlations are determined from the van Hove function

$$G(\mathbf{r},t) = \frac{\langle \rho(\mathbf{r},t)\rho(\mathbf{0},0)\rangle}{\rho} = \frac{1}{N}\left\langle \sum_{i=1}^{N}\sum_{j=1}^{N}\delta[\mathbf{r}-\mathbf{r}_j(0)-\mathbf{r}_i(t)]\right\rangle \tag{5}$$

with $\langle\cdots\rangle$ the ensemble and time average (over many different time origins) calculated from classical MD simulations of an N-particle system, ρ the mean ion density, and $\mathbf{r}_i(t)$ the position of the ith ion at time t. The ion-ion DSF

$$S(\mathbf{k},\omega) = \frac{1}{2\pi}\int_{-\infty}^{\infty} F(\mathbf{k},t)\,e^{i\omega t}dt \tag{6}$$

is the time Fourier transform of the intermediate scattering function $F(\mathbf{k},t)$, which is itself the spatial Fourier transform of the Van Hove function

$$F(\mathbf{k},t) = \int G(\mathbf{r},t)e^{-i\mathbf{k}\cdot\mathbf{r}}d\mathbf{r}. \tag{7}$$

While $G(\mathbf{r},t)$ contains much information relevant to $2T$ situations, $F(\mathbf{k},t)$ is also directly accessible in MD simulations via the relation

$$F(\mathbf{k},t) = \frac{1}{N}\langle \rho_{\mathbf{k}}(t)\rho_{-\mathbf{k}}(0)\rangle, \tag{8}$$

where

$$\rho_{\mathbf{k}}(t) = \sum_{i}^{N} e^{i\mathbf{k}\cdot\mathbf{r}_i(t)}, \tag{9}$$

thus avoiding the calculation of the spatial Fourier transform, which can add spurious high-frequency oscillations to $F(\mathbf{k},t)$ due to the finite size of the MD simulation cell. Under WDM conditions, the averaged system properties are those of an isotropic fluid; thus important structural quantities are spherically symmetric in real space, $|\mathbf{r}| = r$, and in reciprocal space, $|\mathbf{k}| = k$.

In the hydrodynamic limit, $k \to 0$, the DSF takes the so-called "three-peak" form

$$S(k,\omega) = \frac{S(k)}{2\pi}\left[\left(\frac{\gamma-1}{\gamma}\right)\frac{2D_T k^2}{\omega^2 + (D_T k^2)^2}\right.$$
$$+ \frac{1}{\gamma}\left(\frac{\Gamma k^2}{(\omega - c_s k)^2 + (\Gamma k^2)^2}\right.$$
$$\left.\left.+ \frac{\Gamma k^2}{(\omega + c_s k)^2 + (\Gamma k^2)^2}\right)\right] \tag{10}$$

with D_T the thermal diffusivity, Γ the sound attenuation coefficient, $\gamma = c_P/c_V$ the ratio of the constant pressure to the constant volume specific heats (c_p and c_V), and c_s the adiabatic speed of sound. The second and third terms of Eq. (10) are the Brillouin peaks whose positions provide the acoustic dispersion relation $\omega_s(k)$, which is linear at small k, $\omega_s(k \to 0) = c_s k$, and is measurable experimentally. In

addition, it is also possible to compute c_s from the SSF $S(k)$ using the compressibility κ sum rule $S(0) = \rho \kappa T_i$, which leads to $c_s = \sqrt{T_i / S(0)}$. Once the PP is constructed, the SSF can be easily calculated via the MHNC procedure, independent of MD simulations.

C. Equation of state

The total free energy per atom in the NPA model is given by

$$F = F_e^0(T_e) + F_{emb}(T_e) + F_{ii}(T_i, T_e) + F_i^0(T_i), \qquad (11)$$

with contributions F_e^0 from the interacting homogeneous electron gas, F_{emb} from the embedding of the pseudoatom into the uniform system, F_{ii} from the interacting ion-ion system, and F_i^0 from the ideal ion gas. A more detailed description of each term of the NPA free energy is given in Refs. [26,38]. For the equilibrium system, the pressure is obtained via the density derivative of the free energy while the internal energy is obtained by taking the temperature derivative:

$$P = n^2 \frac{\partial F}{\partial n}, \quad E = \frac{\partial (\beta F)}{\partial \beta} \qquad (12)$$

with $\beta = 1/T$. For quasiequilibrium systems, the internal energy must be computed taking into account the temperature derivative of each contribution in Eq. (11). Note that the term F_{ii} depends on both T_i and T_e. Thus, the total derivative of the $2T$ internal energy reads

$$E(T_e, T_i) \equiv \frac{\partial (\beta F)}{\partial \beta} = F + \left. \frac{F}{\partial \beta_e} \right|_{T_i} + \left. \frac{\partial F}{\partial \beta_i} \right|_{T_e}, \qquad (13)$$

which recovers the correct equilibrium internal energy when $T_i = T_e$.

III. RESULTS

All DSF have been calculated from MD simulations using the NPA pair potentials. The initial configuration was a face-centered-cubic crystal containing 5324 particles arranged in a cubic simulation cell. This corresponds approximately to a linear dimension of 17 to 18 Wigner-Seitz radii, i.e., significantly larger than typical ion-ion correlations seen in the ion-ion pair distribution of aluminum even at its melting point. Simulations were carried out over 0.5 ns with a time step of 0.5 fs. The first 50 000 steps have not been used as they pertain to the initial equilibration period. From the remaining simulation, configurations have been extracted every 1 fs for the calculation of $G(r,t)$ and $F(k,t)$, which have been calculated up to 3000 fs. The ion temperature was kept constant throughout the simulation using a Nosé-Hoover thermostat. The electron temperature no longer appears in the dynamics, so no electron thermostat is needed; T_e only intervenes in the construction of the NPA pair potential, which is the essential "quantum input" to the classical MD simulation.

In the range of T_e studied in this work, i.e., from 1 to 10 eV, the mean ionization calculated from the NPA model remained essentially unchanged from the room-temperature value of $\bar{Z} = 3.0000$–3.0163 for the normal density of 2.7 g/cm^3. Given a Fermi energy (i.e., approximately the chemical potential) of ~12 eV, no significant change in $\bar{Z}$ is in fact
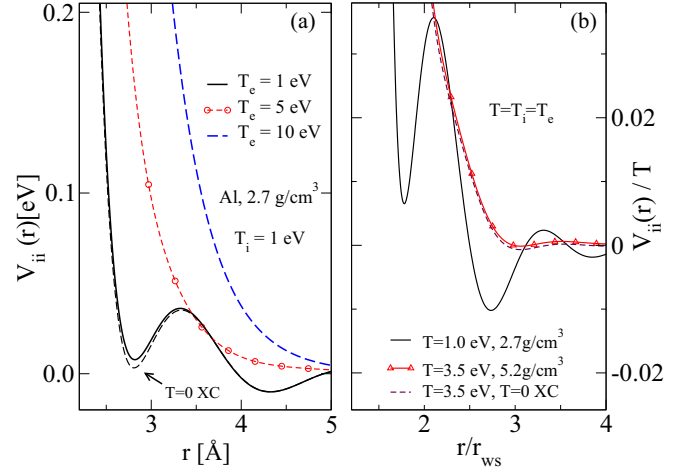

FIG. 1. (a) Ion-ion pair potentials constructed from the NPA model at electron temperatures of $T_e = 1$, 5, and 10 eV, while the ion temperature is held at $T_i = 1$ eV. (b) The $T_i = T_e = 1$ eV potential for the "room-temperature" Al density 2.7 g/cm^3, as well the pair potential at 5.2 g/cm^3 and $T = 3.5$ eV relevant to the work of Rüter and Redmer [11]. Note that in panel (b) we have plotted the potentials in terms of physically relevant variables r/r_{ws} and $V_{ii}(r)/T$, where the nominal WS radii r_{ws} are 2.991 and 2.404 a.u., respectively.

expected. There is even less of a change at the higher density of 5.2 g/cm^3 used by Rüter et al. [11], as the Fermi energy is correspondingly higher. The value of $\bar{Z}$ for Al begins to increase only from about 20 eV, and the consistency of the NPA-evaluated $\bar{Z}$ even at higher temperatures is shown from its successful prediction of electrical conductivities of aluminum under a variety of WDM conditions [23,39].

A. Static properties

We first review the results for several key static properties, viz. pair potentials, PDFs, and structure factors.

1. Pair potentials

The easily computed NPA ion-ion pair potentials described by Eq. (4) are the starting point of our study of the aluminum DSF, using classical molecular dynamics with the NPA-PPs as the input. Hence, in Fig. 1 we show typical Al-Al pair potentials that are relevant to our study. These pair potentials are the simplest that can be constructed from the NPA density, while the NPA calculation provides enough data to construct more complex nonlocal pseudopotentials, or potentials designed to recover phase shifts, etc. However, such elaborations need to be invoked only if such potentials are really required. We have found that this elementary approach works well for simple metallic fluids in regimes of compressions of 0.5 to about 2.5, and from low temperatures (e.g., melting point) to higher temperatures (where the model works better). In the present study (aluminum at 2.7, and 5.2 g/cm^3, at $T = 1$ and 3.5 eV, respectively), the model is eminently applicable, as we show by comparisons with more microscopic simulations for the PDFs and other properties given below. Panels (a) and (b) show the crucial role played by the Friedel oscillations in the potentials. These are evident in the potential at $T_e = 1$ eV

and more weakly in the 3.5 eV potential. At high T_e, they are damped out and the potentials become more Yukawa-like. The NPA model faithfully reproduces these potentials to good accuracy, whereas many commonly used average-atom models do not. The location of these oscillations, as well as packing effects in the fluid, are controlled by r_{ws}. Hence the plot using r/r_{ws} as the x coordinate brings potentials at different densities to a comparable footing. We also show the pair potential at 5.2 g/cm^3 and $T = 3.5$ eV calculated using the $T = 0$ XC functional that is customarily implemented in DFT-MD simulations, showing a small and probably negligible difference. However, it should always be remembered that standard DFT-MD simulations can be used to benchmark other calculations only when the $T = 0$ XC approximation holds.

2. Pair-distribution function

The NPA-PPs are known to closely reproduce the ion-ion PDF $g(r)$ and the corresponding static structure factor $S(k)$ for most systems studied so far, for compressions of 0.5 to about 2.5. Some examples are as follows:

(i) Al (a) at normal density $\rho = 2.7$ g/cm^3 and at the melting point, and (b) at an expanded density $\rho = 2.0$ g/cm^3 with $T = 1000$ and 5000 K [40].

(ii) Li at $T = 2000$ K and $\rho = 0.85$ g/cm^3 [17].

(iii) Be at densities of $\rho = 1.85$ and 5.53 g/cm^3 for various two-temperature situations [8].

(iv) C, Si, and Ge in the WDM state [41,42]. Here, because of the high electron density ($\bar{Z} = 4$), the NPA model works even at 12 g/cm^3, i.e., close to six times the graphite density.

While liquid metal PDFs can be obtained from MD simulations using multicenter potentials such as those available from EM theory [33], embedded-atom model (EAM) approaches [43], or bond-order potentials [44], they have not been applied in an intensive way to the WDM regime. The effect of T_e on the ion-ion interaction is not included except in limited cases [45]. Kraus *et al.* [34] examined the use of multi-ion bond-order potentials for WDM carbon but found them to be unsuitable and extremely difficult to formulate for finite-T usage. In contrast, the NPA-PPs are simple to compute and are at finite-T from the outset. Here we show that the PDFs obtained from them agree closely with those from DFT-MD for the systems studied here.

In Fig. 2, NPA PDFs for aluminum at the "normal" density ρ_0 are compared with DFT-MD simulations from Recoules *et al.* at 10 000 and 30 000 K [46]. The agreement is relatively good. The slight disagreement ($\sim 4\%$) noted near the main peak is a common feature in this type of comparison, arising from statistical noise in MD simulations with, say, $N \sim 100$ atoms. Here one may expect fluctuations of $\sim 1/\sqrt{N}$. In reality, the need to take an ensemble average of every quantity in DFT-MD simulations adds to the labor and cost. In Fig. 3, we compare the PDF for Al obtained from the NPA pair potentials with that from Kohn-Sham DFT-MD simulations for two cases. The first case [panel (a) in Fig. 3] is for the room-temperature density $\rho = 2.7$ g/cm^3 at a temperature $T = 1$ eV, which gives one of the equilibrium WDMs used in this study. The second case [panel (b) in Fig. 3] is for the compressed density $\rho = 5.4$ g/cm^3 at a temperature $T = 3$ eV, which is close to the conditions used by Rüter and Redmer [11] in their
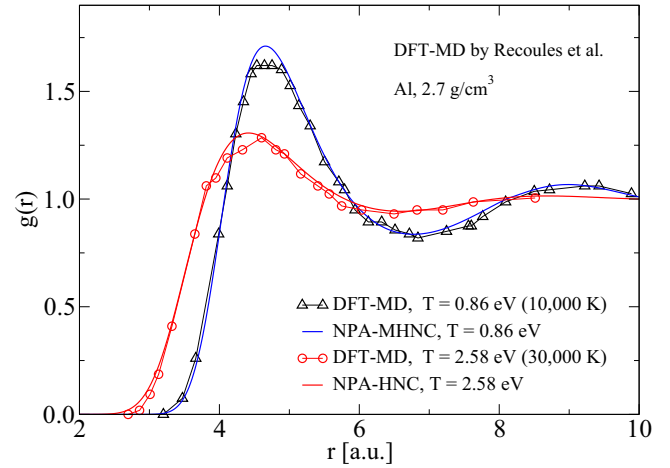

FIG. 2. A comparison of the $g(r)$ from the NPA-MD and from DFT-MD simulations (Recoules *et al.* [46]) for Al at the normal density ρ_0 and at 10 000 and 30 000 K. No bridge terms are needed at the higher T case, where HNC and MHNC become equivalent).

DFT-MD calculation of the aluminum DSF. The latter is used in Sec. III B to compare with our NPA-MD DSF. Our DFT-MD simulations were done with the ABINIT package using a cell of 108 atoms with a norm-conserving pseudopotential and the $T = 0$ Perdew-Burke-Ernzerhof exchange and correlation functional within the generalized gradient approximation. In this case, the positions of the first maxima in $g(r)$ are within 1% of each other for the first case (a) and within 2% for the second case (b). The height of the first peak differs by about 3% in both cases, showing the good agreement between DFT-MD and NPA-MD simulations. The use of pair potentials to perform classical MD simulations requires a considerably shorter amount of time, illustrating the advantage of employing the NPA model.
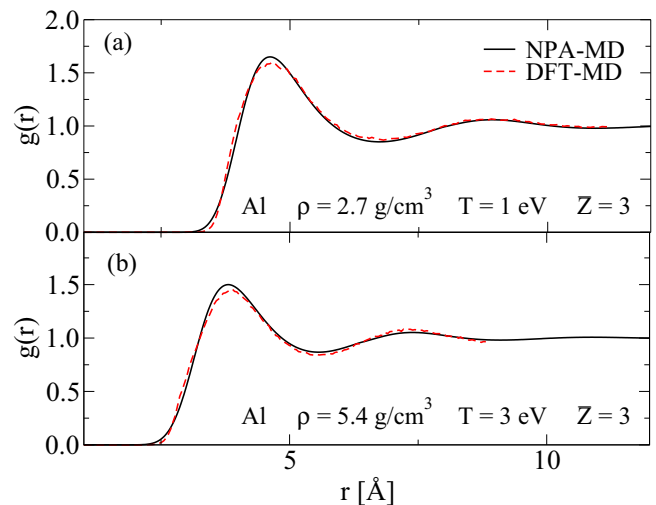

FIG. 3. Comparison of the $g(r)$ from the NPA-MD and from DFT-MD simulations for two Al WDM states: (a) ρ at the room-temperature density of 2.7 g/cm^3, $T = 1$ eV and (b) $\rho = 5.4$ g/cm^3, $T = 3$ eV.
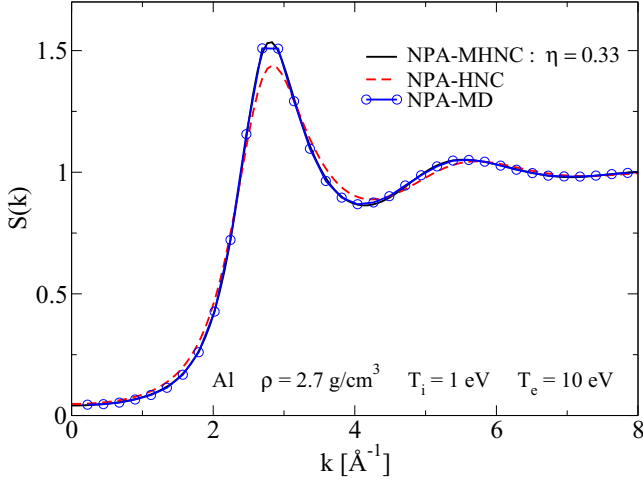
FIG. 4. $S(k)$ computed from MHNC (continuous line), HNC (red dashed line), and MD (blue circles and blue line) simulations at $T_i = 1$ eV and $T_e = 10$ eV.

3. Static structure factor

As indicated in Sec. II B, c_s can also be calculated from the SSF using the compressibility sum rule. In Fig. 4, we compare the $S(k)$ computed from HNC, MHNC, and MD simulations all using the same pair potential. We note that the MHNC SSF and the MD SSF agree very well, while the HNC predicts a slightly lower maximum and a slightly different $k = 0$ limit. This suggests that the differences may be due to the use of a hard-sphere model within the Lado-Foiles-Ashcroft criterion for modeling the bridge function [47]. In principle, more accurate bridge functions can be extracted from MD simulations.

B. Dynamical properties

1. Dynamical structure factor: Equilibrium system

In this section, the DSF for equilibrium Al, $T_i = T_e$, obtained from the NPA-PP, is compared with other DSF calculations. First we consider the results of Rüter and Redmer [11], who used Kohn-Sham DFT-MD to study Al at a density of $\rho = 5.2$ g/cm^3 (compression $\sim$2) and $T = 3.5$ eV, i.e., $T/E_f \simeq 0.19$. In Fig. 5, the NPA-MD DSF is compared with the DFT-MD DSF for $k = 0.42$ and 0.69 Å^{-1}. The position and profile of the Brillouin peak obtained from the NPA-MD agree closely with results from DFT-MD. Furthermore, the speed of sound obtained by Rüter and Redmer, $c_s = 10.38$ km/s, and the NPA value of $c_s = 10.62$ km/s are within 2.3% of each other. In this case, the NPA calculation satisfies the f-sum rule to within 96% over the range of k studied.

Since a full Kohn-Sham DFT-MD calculation as given by Rüter et al. [11] for the DSF is extremely costly, simpler approaches based on average-atom models as well as orbital-free methods have been used to compute the ion-ion DSF. Here we compare the results from the NPA-MD with corresponding results from the pseudoatom model of Starrett and Saumon [48] (PA-SS), and with OF-DFT-MD simulations, for Al at the density ρ_0 and $T = 5$ eV. A comparison of our NPA-MD calculations with the OF-DFT-MD simulations of White et al.
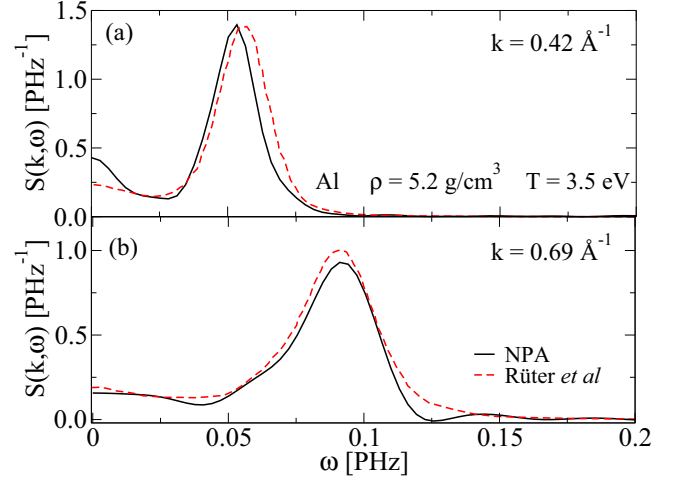

FIG. 5. A comparison of the dynamic structure factors obtained from NPA-MD (this work) and DFT-MD [11] at two different wave vectors. In NPA-MD, the pair potential [Eq. (4)] is the input to simulation.

[20] and those of Gill et al. [49], using the PA-SS and MD, is presented in Fig. 6 for wave vectors $k = 0.45$ and 0.96 Å^{-1}. White et al. used 108 ions in a cubic supercell in an OF-DFT approach. Gill et al. presented an OF model calculation with a classical simulation with 10 000 ions, and also a Kohn-Sham (KS) approach within their PA-SS model. Since our NPA model uses the KS procedure, only the KS-PA-SS results are compared in Fig. 6.

The positions of the Brillouin peak for $k = 0.45$ Å^{-1} coincide for OF-DFT-MD and NPA-MD, and the peak heights differ by $\sim$4%. The adiabatic speed of sound $c_s = \omega_s/k$ was obtained by a linear fit to the dispersion relation $\omega_s(k)$ for a small value of k. The OF-DFT-MD predicts an adiabatic speed of sound of 10.4 km/s, very close to the NPA-MD
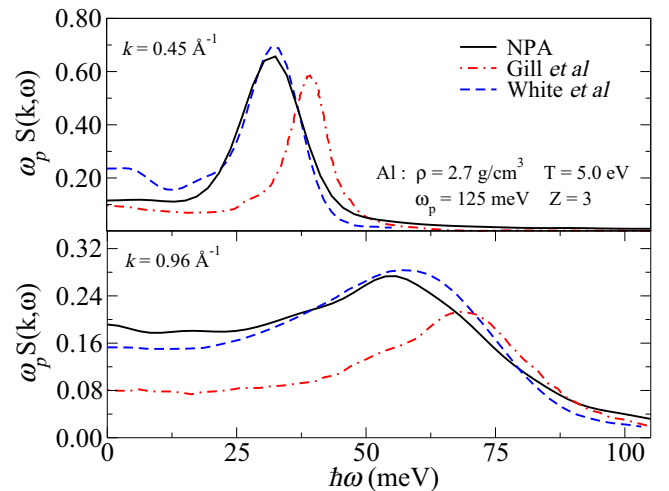

FIG. 6. The equilibrium DSF of Al at density $\rho = \rho_0$ and $T = 5$ eV, for wave vector $k = 0.45$ Å^{-1} (upper panel) and 0.96 Å^{-1} (lower panel): NPA (black continuous line), PA-SS [49] (red dot-dashed line), and OF-DFT-MD [20] (blue dashed line).
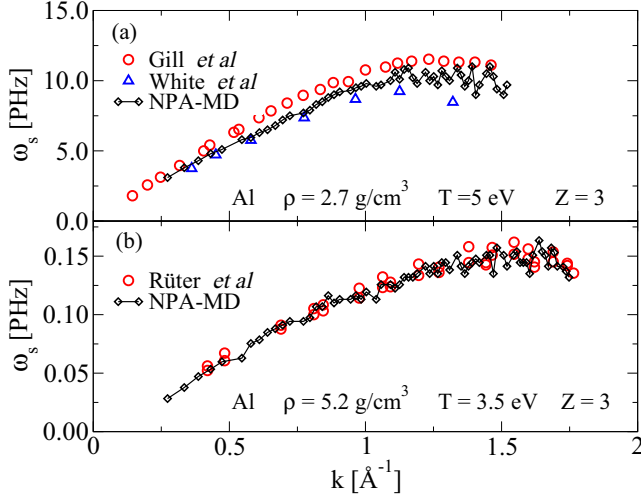
FIG. 7. A comparison of the equilibrium acoustic dispersion relation of Al for (a) density $\rho = \rho_0$ and $T = 5$ eV as in the OF-DFT-MD calculations of White *et al.* [20] and as in the PA-SS calculations of Gill *et al.* [49], and (b) $\rho = 5.2$ g/cm^3 and $T = 3.5$ eV as in Rüter *et al.* [11].
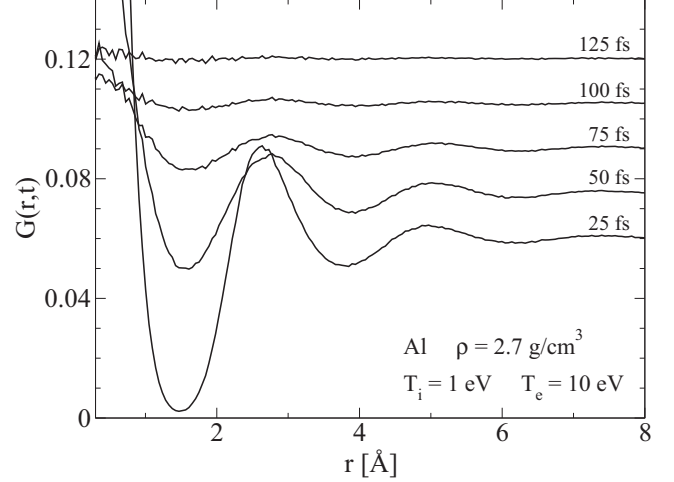

FIG. 8. The Van Hove function for different times for the case $T_i = 1$ eV and $T_e = 10$ eV. For clarity, each curve is shifted vertically by 0.015 from the previous one while the curve for $t = 25$ fs is unshifted.

value of 10.2 km/s, whereas the PA-SS-MD predicts a higher value of 12.7 km/s (see Fig. 7). Once again, we ensured that the NPA calculation satisfies the f-sum rule to within 97% over the range of k studied. The good agreement between the equilibrium DSF calculated via the NPA-MD and OF-DFT-MD mutually confirms the extent of validity of these methods and of the NPA-MD approach. We already noted the good agreement with the fully microscopic calculations of Rüter *et al.* [11]. All these encourage us to apply $2T$-NPA-PP to investigate the dynamical properties of quasiequilibrium systems where $T_e \neq T_i$.

2. Dynamical structure factor: Quasiequilibrium system

To study the ion dynamics in the quasiequilibrium system with $T_e > T_i = 1$ eV, we employ the ion-ion pair potential $V_{ii}(r, T_e)$ constructed from the NPA calculation, which explicitly depends directly on T_e. The dependence on T_i comes in via the ion density and the ionization state $\bar{Z}$ of the ions, and hence is implicitly included in the NPA calculation. In Fig. 1(a) we present the potentials for the cases $T_e = 1, 5,$ and 10 eV. At $T_e = 1$ eV, the potential exhibits Friedel oscillations with several minima, whereas it becomes purely repulsive at higher temperatures since the Fermi energy at 2.7 g/cm^3 is 11.65 eV.

To ensure that the two-temperature DSF of the quasiequilibrium system is physically relevant, we must verify that all spatial correlations vanish in a time τ_c smaller than the ion-electron relaxation time τ_{ei}, which is of the order of hundreds of picoseconds [50]. The Van Hove function has been calculated for the specific case $T_i = 1$ eV and $T_e = 10$ eV, and its time evolution is presented in Fig. 8. We find that at $\tau_c = 125$ ps, all spatial correlations have vanished, such that $\tau_c < \tau_{ei}$, implying that dynamical properties can be meaningfully calculated for the quasiequilibrium system.

The $2T$-DSF at $\rho = \rho_0$, computed with the NPA-based PP, is presented in Fig. 9 for $T_i = 1$ eV and $T_e = 1, 5,$ and 10 eV,

and wave vector $k = 0.45$ Å^{-1}. The position of the Brillouin peak shifts to higher ω as T_e increases while the value at $\omega = 0$ is drastically lowered. Furthermore, the shape of the peak is narrower for higher T_e.

The dispersion relation $\omega_s(k)$ for $T_e = 1, 5,$ and 10 eV can be deduced from the position of the Brillouin peak. It is displayed in Fig. 10.

The dispersion relation begins to be noisy and unphysical at different values of wave vector k as T_e is increased. Thus the position of the Brillouin peak could be confidently determined only up to $k = 0.8, 1.2,$ and 1.5 Å^{-1} for $T_e = 1, 5,$ and 10 eV, respectively. Establishing that collective excitations still exist for higher values of k becomes more difficult as the Brillouin peak merges back with the Rayleigh peak at $k = 0$. This makes it hard to evaluate the full width at half-maximum of the Brillouin peak, ideally needed to establish the survival
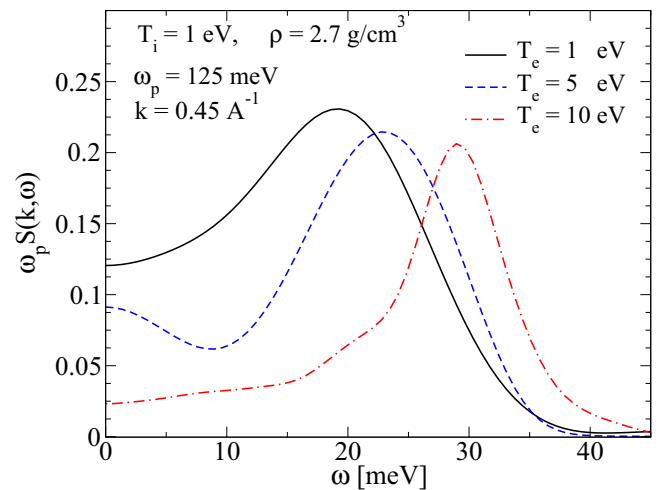

FIG. 9. The quasiequilibrium DSF of Al at density ρ_0, $T_i = 1$ eV and $T_e = 1, 5, T = 10$ eV for wave vector $k = 0.45$ Å^{-1}.
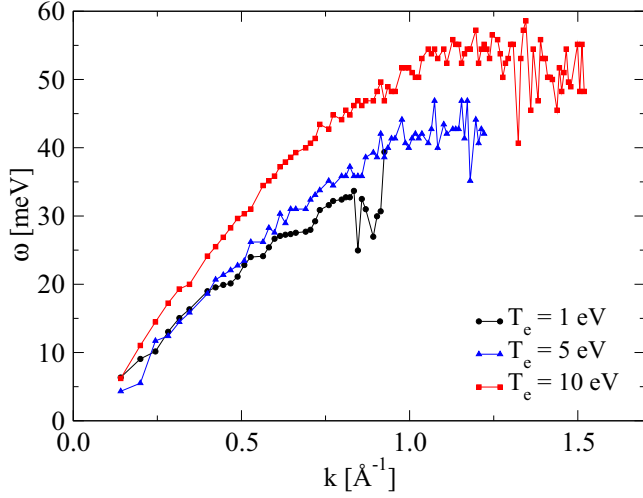
FIG. 10. The two-temperature dispersion relation $\omega_s(k)$ calculated from the position of the Brillouin peak for $T_i = 1$ eV and $T_e = 1$, 5, and 10 eV.

of longitudinal modes at higher k and higher T_e. Instead, we decided to include the position of the peak as long as its height is at least 20% higher than the value at $k = 0$. Using the same procedure for each combination of T_i and T_e enables us to treat them in a comparable manner. Longer MD simulations would yield better results for $\omega_s(k)$; however, the current results are sufficiently precise to conclude that there exist more ion longitudinal modes at $T_e = 10$ eV than at lower T_e; this may be due to the lower compressibility of the electron subsystem as well as the ion subsystem with a more repulsive pair potential, as shown in Fig. 1, the ion temperature being identical. These dispersion relations will be used to determine the speed of sound c_s as a function of T_e. Predictions of the speed of sound computed from the DSF, the MHNC-SSF, and the HNC-SSF are compared in Fig. 11.

The speed of sound calculated from the DSF is slightly and systematically higher than the MHNC-SSF value through the entire range of T_e, with a maximum difference of 4.6% occurring at $T_e = 7$ eV; both methods predict a 43% increase from $T_e = 1$ to 10 eV. These results also confirm the phenomenon of phonon hardening [18]. It should be noted that the HNC-SSF value is considerably lower than the value from other methods,
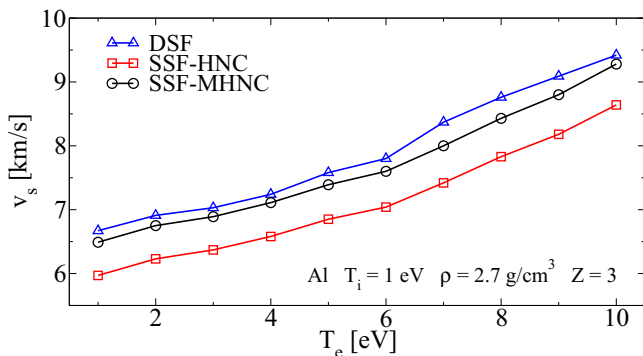

FIG. 11. Comparison of the speed of sound in the $2T$ system calculated from the SSF and from the DSF with $T_i = 1$ eV.
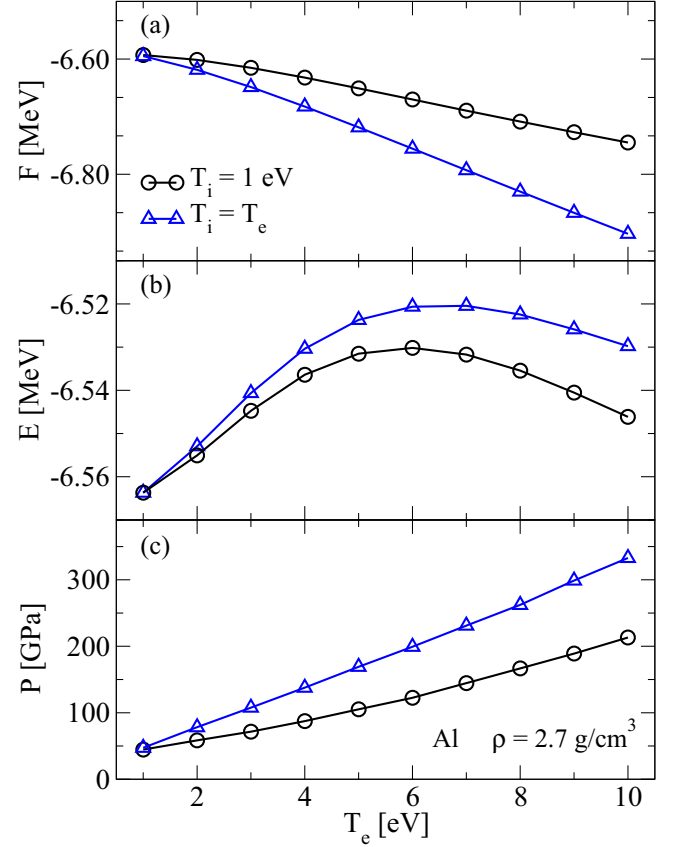

FIG. 12. Comparison between the equilibrium and quasiequilibrium free energy (a), internal energy (b), and pressure (c) of Al at density ρ_0. As T_i is held fixed at 1 eV for quasiequilibrium time scales (or longer via a thermostat coupled only to the ions), the ionic lattice does not expand and the density remains fixed.

illustrating the importance of using a bridge term in the integral equation for the ion distribution at these coupling strengths.

C. Quasiequation of state

The NPA model allows a rapid calculation of the EOS of Al in equilibrium conditions, which was intensively investigated by Sjostrom *et al.* [51], but also for $2T$ situations. In Fig. 12 we present a comparison between the equilibrium and the quasiequilibrium Helmholtz free energy F, internal energy E, and total pressure P. At the highest electronic temperature ($T_e = 10$ eV) that we have studied, the equilibrium F is lower than that of the quasiequilibrium system by 2.3% while the internal energy is higher by 0.25%. The internal energy in both cases has a maximum in the range of $T_e = 6$–7 eV and has a similar shape. While F and E are only slightly modified in the $2T$ regime, the equilibrium pressure is higher than that obtained at quasiequilibrium by as much as 56% at $T_e = 10$ eV. Even though the changes in the free energy and internal energy are small, such variations could considerably affect EOS-dependent properties such as specific heats, conductivities, energy relaxation rates, and other coupling coefficients that enter into more macroscopic WDM simulations. The efficiency and rapidity of computing such $2T$-EOS via the NPA model allows us to obtain them on the fly for simulations of shocked or

laser-driven systems, for most combinations of T_i and T_e where a significant density of free electrons is available to make the NPA approach valid, and where no persistent chemical bonds are formed.

IV. CONCLUSION

Taking aluminum as an example, we demonstrated that the NPA pair potentials can be used to compute efficiently and accurately the equilibrium dynamic structure factor via MD simulations, and we established that it is in close agreement with DFT-MD results. We explored the two-temperature system and showed that all ion-ion correlations vanish in a time shorter than typical electron-ion relaxation times, validating the concept of a $2T$-dynamic structure factor in this context.

We presented the $2T$-DSF and showed that the Brillouin peak shifts to higher energies as the electron temperature is increased. As a result, the ion acoustic mode dispersion relation is modified and the adiabatic speed of sound c_s is increased, in good agreement with its determination via the compressibility sum rule in the small-k limit of the static structure factor. The latter is independently obtained via the modified hypernetted-chain method and using the pair potentials generated via

the neutral-pseudoatom method. The increase in the acoustic velocity is also consistent with the phenomenon of "phonon hardening."

The comparison between the equilibrium and quasiequilibrium EOS shows that the free energy and the internal energy are only weakly modified in the two-temperature system, while the pressure is significantly affected. The efficient calculation of the quasiequilibrium EOS via the neutral pseudoatom method constitutes a powerful tool for exploring out-of-equilibrium systems via MD simulations.

[1] T. Guillot, Science **286**, 72 (1999).
[2] P. Lorazo, L. J. Lewis, and M. Meunier, Phys. Rev. Lett. **91**, 225502 (2003).
[3] S. Atzeni and J. Meyer-ter Vehn, *The Physics of Inertial Fusion: Beam-Plasma Interaction, Hydrodynamics, Hot Dense Matter* (Clarendon, Oxford, 2004).
[4] L. B. Fletcher, H. J. Lee, T. Döppner, E. Galtier, B. Nagler, P. Heimann, C. Fortmann, S. LePape, T. Ma, M. Millot, A. Pak, D. Turnbull, D. A. Chapman, D. O. Gericke, J. Vorberger, T. White, G. Gregori, M. Wei, B. Barbrel, R. W. Falcone, C.-C. Kao, H. Nuhn, J. Welch, U. Zastrau, P. Neumayer, J. B. Hastings, and S. H. Glenzer, Nat. Photon. **9**, 274 (2015).
[5] T. Ma, T. Döppner, R. W. Falcone, L. Fletcher, C. Fortmann, D. O. Gericke, O. L. Landen, H. J. Lee, A. Pak, J. Vorberger, K. Wünsch, and S. H. Glenzer, Phys. Rev. Lett. **110**, 065001 (2013).
[6] H. J. Lee, P. Neumayer, J. Castor, T. Döppner, R. W. Falcone, C. Fortmann, B. A. Hammel, A. L. Kritcher, O. L. Landen, R. W. Lee, D. D. Meyerhofer, D. H. Munro, R. Redmer, S. P. Regan, S. Weber, and S. H. Glenzer, Phys. Rev. Lett. **102**, 115001 (2009).
[7] M. W. C. Dharma-wardana, Phys. Rev. E **93**, 063205 (2016).
[8] L. Harbour, M. W. C. Dharma-wardana, D. D. Klug, and L. J. Lewis, Phys. Rev. E **94**, 053211 (2016).
[9] S. H. Glenzer and R. Redmer, Rev. Mod. Phys. **81**, 1625 (2009).
[10] J. Chihara, J. Phys. F **17**, 295 (1987).
[11] H. R. Rüter and R. Redmer, Phys. Rev. Lett. **112**, 145007 (2014).
[12] J. Clérouin, G. Robert, P. Arnault, C. Ticknor, J. D. Kress, and L. A. Collins, Phys. Rev. E **91**, 011101 (2015).
[13] J. Vorberger and D. O. Gericke, Phys. Rev. E **91**, 033112 (2015).
[14] A. D. Baczewski, L. Shulenburger, M. P. Desjarlais, S. B. Hansen, and R. J. Magyar, Phys. Rev. Lett. **116**, 115004 (2016).

[15] J. P. Hansen and I. R. McDonald, *Theory of Simple Liquids* (Elsevier Science, Amsterdam, 2006).
[16] L. Harbour, M. W. C. Dharma-wardana, D. D. Klug, and L. J. Lewis, Contrib. Plasma Phys. **55**, 144 (2015).
[17] L. Harbour, M. W. C. Dharma-wardana, D. D. Klug, and L. J. Lewis, Phys. Rev. E **95**, 043201 (2017).
[18] V. Recoules, J. Clérouin, G. Zérah, P. M. Anglade, and S. Mazevet, Phys. Rev. Lett. **96**, 055503 (2006).
[19] Y. Hou, Y. Fu, R. Bredow, D. Kang, R. Redmer, and J. Yuan, High Energy Density Phys. **22**, 21 (2017).
[20] T. G. White, S. Richardson, B. J. B. Crowley, L. K. Pattison, J. W. O. Harris, and G. Gregori, Phys. Rev. Lett. **111**, 175002 (2013).
[21] F. Nardin, G. Jacucci, and M. W. C. Dharma-wardana, Phys. Rev. A **37**, 1025 (1988).
[22] M. W. C. Dharmawardana, Contrib. Plasma Phys. **55**, 85 (2015).
[23] M. W. C. Dharma-wardana, D. D. Klug, L. Harbour, and L. J. Lewis, Phys. Rev. E **96**, 053206 (2017).
[24] L. Dagens, J. Phys. C **5**, 2333 (1972).
[25] L. Dagens, J. Phys. France **36**, 521 (1975).
[26] F. Perrot, Phys. Rev. E **47**, 570 (1993).
[27] M. W. C. Dharma-wardana and F. Perrot, Phys. Rev. A **26**, 2096 (1982).
[28] F. Perrot and M. W. C. Dharma-wardana, Phys. Rev. B **62**, 16536 (2000).
[29] M. W. C. Dharma-wardana, Computation **4**, 16 (2016).
[30] F. Perrot, Y. Furutani, and M. W. C. Dharma-wardana, Phys. Rev. A **41**, 1096 (1990).
[31] M. S. Murillo, J. Weisheit, S. B. Hansen, and M. W. C. Dharma-wardana, Phys. Rev. E **87**, 063113 (2013).
[32] M. W. C. Dharma-wardana, Phys. Rev. E **86**, 036407 (2012).

[33] A. E. Depristo, *Recent Advances in Density Functional Methods I: Evaluation and Application of Corrected Effective Medium Methods* (World Scientific, Singapore, 2011), pp. 193–218.

[34] D. Kraus, J. Vorberger, D. O. Gericke, V. Bagnoud, A. Blažević, W. Cayzac, A. Frank, G. Gregori, A. Ortner, A. Otten, F. Roth, G. Schaumann, D. Schumacher, K. Siegenthaler, F. Wagner, K. Wünsch, and M. Roth, Phys. Rev. Lett. **111**, 255501 (2013).

[35] M. W. C. Dharma-wardana, in *Density Functional Theory*, edited by E. K. U. Gross and R. M. Dreizler, Vol. 337 of NATO ASI Series (Plenum, New York, 1993), pp. 625–650.

[36] X. Gonze, B. Amadon, P.-M. Anglade, J.-M. Beuken, F. Bottin, P. Boulanger, F. Bruneval, D. Caliste, R. Caracas, M. Côté, T. Deutsch, L. Genovese, P. Ghosez, M. Giantomassi, S. Goedecker, D. R. Hamann, P. Hermet, F. Jollet, G. Jomard, S. Leroux, M. Mancini, S. Mazevet, M. J. T. Oliveira, G. Onida, Y. Pouillon, T. Rangel, G.-M. Rignanese, D. Sangalli, R. Shaltaf, M. Torrent, M. J. Verstraete, G. Zerah, and J. W. Zwanziger, Comput. Phys. Commun. **180**, 2582 (2009).

[37] G. Kresse and J. Furthmüller, Phys. Rev. B **54**, 11169 (1996).

[38] F. Perrot and M. W. C. Dharma-wardana, Phys. Rev. E **52**, 5352 (1995).

[39] J. F. Benage, W. R. Shanahan, and M. S. Murillo, Phys. Rev. Lett. **83**, 2953 (1999).

[40] M. W. C. Dharma-wardana, Phys. Rev. E **73**, 036401 (2006).

[41] M. W. C. Dharma-wardana, Contrib. Plasma Phys. **58**, 128 (2018).

[42] M. W. C. Dharma-wardana and F. Perrot, Phys. Rev. Lett. **65**, 76 (1990).

[43] Y. Waseda, *The Structure of Non-crystalline Materials: Liquids and Amorphous Solids* (McGraw-Hill, New York, 1980).

[44] L. M. Ghiringhelli, J. H. Los, A. Fasolino, and E. J. Meijer, Phys. Rev. B **72**, 214103 (2005).

[45] S. Khakshouri, D. Alfè, and D. M. Duffy, Phys. Rev. B **78**, 224304 (2008).

[46] V. Recoules, J. Bouchet, M. Torrent, and S. Mazevet, *Report: Ab Initio calculations of X-ray Absorption Spectra for Warm Dense Matter* (CEA, Arpajon, France, 2015).

[47] F. Lado, S. M. Foiles, and N. W. Ashcroft, Phys. Rev. A **28**, 2374 (1983).

[48] C. E. Starrett and D. Saumon, Phys. Rev. E **92**, 033101 (2015).

[49] N. M. Gill, R. A. Heinonen, C. E. Starrett, and D. Saumon, Phys. Rev. E **91**, 063109 (2015).

[50] M. W. C. Dharma-wardana, Phys. Rev. E **64**, 035401 (2001).

[51] T. Sjostrom, S. Crockett, and S. Rudin, Phys. Rev. B **94**, 144101 (2016).